Analyses of microstructural variation in the human striatum using non-negative matrix factorization

Corinne Robert [a,*], Raihaan Patel [a,c], Nadia Blostein [a,b], Chrisopher C. Steele [e,f], M. Mallar Chakravarty [a,b,c,d,**]

[a] Cerebral Imaging Centre, Douglas Mental Health University Institute, Verdun, QC, Canada
[b] Integrated Program in Neuroscience, McGill University, Montreal, QC, Canada
[c] Department of Biological and Biomedical Engineering, McGill University, Montreal, QC, Canada
[d] Department of Psychiatry, McGill University, Montreal, QC, Canada
[e] Department of Psychology, Concordia University, Montreal, QC, Canada
[f] Department of Neurology, Max Planck Institute for Human Cognitive and Brain Sciences, Leipzig, Germany

ABSTRACT

The striatum is a major subcortical connection hub that has been heavily implicated in a wide array of motor and cognitive functions. Here, we developed a normative multimodal, data-driven microstructural parcellation of the striatum using non-negative matrix factorization (NMF) based on multiple magnetic resonance imaging-based metrics (mean diffusivity, fractional anisotropy, and the ratio between T1- and T2-weighted structural scans) from the Human Connectome Project Young Adult dataset ($n = 329$ unrelated participants, age range: 22–35, F/M: 185/144). We further explored the biological and functional relationships of this parcellation by relating our findings to motor and cognitive performance in tasks known to involve the striatum as well as demographics. We identified 5 spatially distinct striatal components for each hemisphere. We also show the gain in component stability when using multimodal versus unimodal metrics. Our findings suggest distinct microstructural patterns in the human striatum that are largely symmetric and that relate mostly to age and sex. Our work also highlights the putative functional relevance of these striatal components to different designations based on a Neurosynth meta-analysis.

1. Introduction

The striatum is a deep grey matter nucleus known to be implicated in motor control (Rolls, 1994) and various executive and cognitive functions,including: goal-directed decision making (Haber et al., 2006a; Stott and Redish, 2014), reward and motivation (van den Bos et al., 2014; Haber et al., 2006a; Jung et al., 2014; Pauli et al., 2016), habitual motor learning (Graybiel and Grafton, 2015) and emotional regulation (Hare et al., 2005). Variation in striatal structure and function have been implicated in various brain disorders including Parkinson's disease (Albin et al., 1989; Hacker et al., 2012), Huntington's disease(Rosenblatt and Leroi, 2000), addiction (Graybiel and Grafton, 2015; Li et al., 2015; Yager et al., 2015), obsessive-compulsive disorders (Graybiel and Rauch, 2000; Milad and Rauch, 2012; Shaw et al., 2015), autism spectrum disorder (Schuetze et al., 2016), and schizophrenia (Chakravarty et al., 2015). Thus, the spatial subdivision of the striatum into regions informed by neuroanatomy is essential to relating striatal

anatomy to function and behaviour. Previous parcellations of this important structure have leveraged magnetic resonance imaging (MRI) data using a combination of heuristic and contrast-based definitions (Burrer et al., 2020; Caravaggio et al., 2018; Leh et al., 2007; Lehéricy et al., 2004). To overcome limitations inherent to these subjective definitions, data-driven parcellations based on structural connectivity (Draganski et al., 2008; Parkes et al., 2017; Tziortzi et al., 2014), resting-state functional connectivity, (Choi et al., 2012; Janssen et al., 2015; Jung et al., 2014; Marquand et al., 2017) and task-based functional connectivity (Pauli et al., 2016) have been proposed. However, the existing parcellations have failed to characterize the tissue microstructure that necessarily constrains the organization and functional variation of the striatum.

In previous work, microstructural aspects of brain organization have been captured using structural and diffusion metrics derived from magnetic resonance imaging (MRI). Such microstructural metrics included the ratio between T1-weighted and T2-weighted images (T1w/T2w) (Glasser et al., 2016; Glasser and Van Essen, 2011; Patel et al., 2020; Tardif et al., 2016; Tullo et al., 2019), fractional anisotropy (FA)

(Alexander et al., 2007; Lebel et al., 2008; Patel et al., 2020; Tardif et al., 2016) and mean diffusivity (MD) (Lebel et al., 2008; Patel et al., 2020; Tardif et al., 2016). Typically these indices are used in isolation. The main goal of this study is to develop a data-driven microstructural parcellation of the striatum using a combination of T1w/T2w, FA and MD, and to link inter-individual variations in the obtained microstructural pattern to behaviour and demographics. We will be using a framework previously developed and thoroughly investigated in Patel et al. (2020) that used a similar approach to develop a multimodal parcellation of the human hippocampus using non-negative matrix factorization (NMF). The uncovered spatially distinct hippocampal parcels were found to be microstructurally distinct and stable across subjects.

We hypothesize that the decomposition of the covariance between the T1w/T2w, FA and MD metrics should yield parcels of the striatum that are more stable across our subjects relative to a decomposition based on a single metric. (Patel et al., 2020; Sotiras et al., 2015). Finally, we aim to relate group-level microstructural patterns of the striatum to brain function through a functional MRI (fMRI) based platform called Neurosynth (Yarkoni et al., 2011).

2. Methods and materials

2.1. Overview

A schematic illustration of the methods of analyses used in the present study can be found in Fig. 1. We used structural and diffusion MRI data from the Human Connectome Project (Section 2.2). The striatum segmentations were generated automatically using the Multiple Automatically Generated Templates (MAGeT) Brain algorithm (Section 2.2.3). A population average constructed using the T1w and T2w images of each subjects was also generated to provide a common space for the microstructural metrics used in our analyses (Section 2.2.4). The obtained striatal labels, T1w/T2w, FA and MD maps to this common space to construct the input matrices that then underwent NMF decomposition (Section 2.3.1, Fig. 1A–C). A stability analysis was performed to find the optimal number of components (Section 2.4) and the final solution was compared to unimodal solutions. The final multi-modal NMF solution was used to generate neuroanatomically distinct clusters that are used to describe the microstructural anatomy of the striatum (Section 2.3, Fig. 1D). Then, we use the inter-indiviual variability in the striatal components, characterized by the NMF subject-level weights (Section 2.3, Fig. 1E) to understand how patterns of covariance may relate to behaviour and demographics using Partial Least Squares correlation analysis (Section 2.5, Fig. 1G). Finally, to ascertain their putative functional relevance, these clusters were used as input to Neurosynth meta-analytical decoder to compare them to meta-analyzed fMRI findings (Section 2.7, Fig. 1F).

2.2. Data

We used multimodal MRI along with behavioural and demographic data from the Human Connectome Project (HCP) Young Adult dataset. We selected structural and diffusion MRI data from 333 unrelated subjects (from a cohort of 1086 twin and non-twin siblings) with age ranging from 22 to 35 years (Van Essen et al., 2013). Most of the participants were individuals born in Minnesota and participants were excluded for severe neurodevelopmental, neuropsychiatric or neurologic disorders (Van Essen et al., 2013). All structural and diffusion MRI data were acquired on a customized Siemens 3T Skyra scanner with a 100 mT/m gradient (Van Essen et al., 2013).

2.2.1. T1w/T2w images

We used preprocessed T1 (T1w)- and T2-weighted (T2w) images from the HCP database (0.7 mm isotropic images) (Van Essen et al., 2013). T1w images were further preprocessed using the minc-bpipe library minc-bpipe library to perform intensity non-uniformity correction,

cropping of the neck region and brain mask generation. T1w images were used to derive a minimally-biased group template (as described below) and the T1w/T2w images were used as a putative measure of voxel-wise myelin content (Glasser and Van Essen, 2011; Tullo et al., 2019). Detailed preprocessing of the HCP data is described in detail elsewhere (Glasser et al., 2013; Van Essen et al., 2013).

2.2.2. DWI scalars

The preprocessed diffusion weighted imaging data (1.25 mm isotropic voxel dimensions) were also downloaded via the HCP online portal. The processing pipeline applied to the diffusion data by the HCP is described in Glasser et al. (2013). The diffusion data were further processed by R.P. in another study from our group (Patel et al., 2020) with MRtrix (Tournier et al., 2012) to estimate MD and FA maps for each subject. To do so, single shell ($b = 1000$) data was used to construct the tensor with weighted least-squares (Basser et al., 1994a) and iterated least-squares (Veraart et al., 2013) using the dwi2tensor command. Then, the MD and FA maps were estimated from the tensor using the tensor2metric command (Basser et al., 1994b; Westin et al., 1997). Note that the structural and diffusion data was already in the T1W space as per the HCP processing pipeline (Glasser et al., 2013).

2.2.3. Automatic striatum segmentation

The striatum was segmented in each subject's T1w image using the publicly available MAGeT brain algorithm (Chakravarty et al., 2013). We used 5 high-resolution manually segmented subcortical atlases based on the reconstruction of serial histological data (Chakravarty et al., 2006; Tullo et al., 2018). All registrations in this section and the next section were performed using the Automatic Normalization Registration Tools (ANTs) (Avants et al., 2010). Two runs of MAGeT brain were performed by N. B. on the entire HCP cohort ($N = 1086$): manual quality control of the outputs from the first run allowed for the selection of the 21 subjects with the best segmentations; these subjects were then used as templates for the second and final run. This allowed for more subjects to obtain a perfect score of 1 for the MAGeT's generated labels and thus pass manual quality control for output quality (see the guide). MAGeT brain was run separately for each hemisphere by isolating the left and right striatum labels in the 5 subcortical atlases to account for anatomical asymmetries and to improve segmentation accuracy a strategy which is been successfully used elsewhere (Chakravarty et al., 2008).

2.2.4. Population average

A population average was used to obtain a voxel-wise correspondence between our 333 subjects and was computed by R.P. in another study from our group (Patel et al., 2020). We used the transformation files from the T1w images to the common space to warp each subject's striatum segmentation and applied the same transformation to T1w/T2w, FA and MD images to the common space using the antsApplyTransforms command. All the images warped to the common space had 1.2 mm isotropic voxel dimensions. T1w/T2w images were filtered using a Gaussian weighted average to remove any outlier values (Glasser and Van Essen, 2011; Patel et al., 2020).

Striatum labels that passed quality control (left, $n = 252$; right, $n = 289$) were transformed to the common space and a unified label was generated by voxel-wise majority vote. The final labels were adjusted for over-segmentation in areas such as the lateral ventricle or the internal capsule (see examples here) to minimize partial voluming effects of ventricles. Although some subjects failed the striatum segmentation, all participants in this study passed the manual QC of the registration of our subjects to the population average. All the following analyses were performed in the common space using the unified labels. See the supplement for more information on the majority voted striatum labels.

2.3. Non-negative matrix factorization

We used an orthonormal projective variant of non-negative matrix factorization (OPNMF). This method provides a part-based decompo-
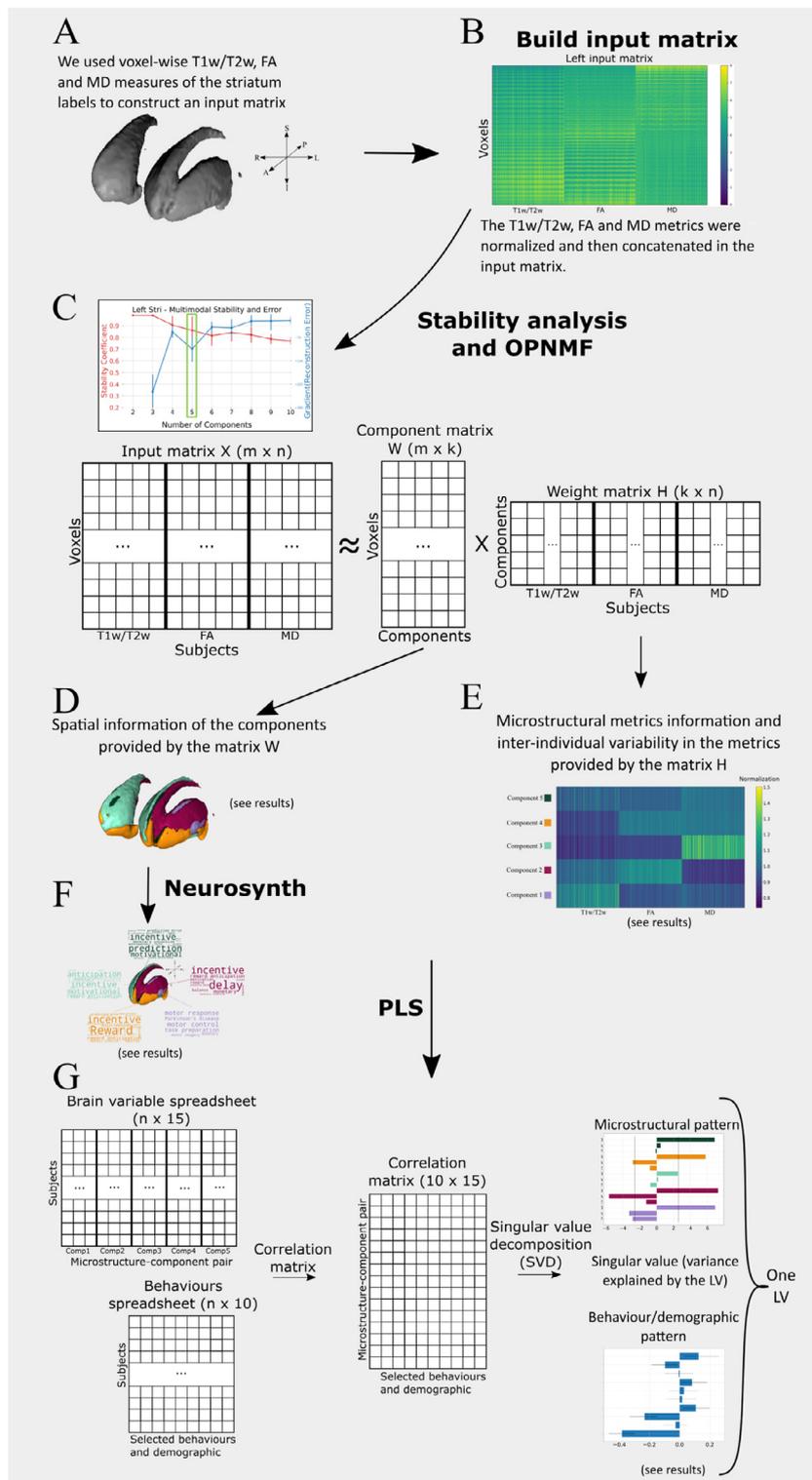
Fig. 1. Workflow A) We used the chosen microstructural metrics in automatically segmented striatum labels (obtained with the MAGeT Brain algorithm) of our subjects in the a constructed common space B) We concatenated the striatal voxels in column vectors of all our subjects to build an input matrix. The left and right input matrix were build independently. C) We extracted spatially distinct components representing patterns of covariance in microstructure across subjects using orthogonal projective non-negative matrix factorization (OPNMF). OPNMF decomposes an input matrix into a component matrix W and a weight matrix H. As OPNMF extracts a predefined number of component k, we performed a stability analysis to assess the accuracy and spatial stability at each granularity from 2 to 10 (see Fig. 2A). D) The component matrix W describes how much each voxel weight into a specific component providing spatial information about the clusters. F) We related each component to functional MRI findings by using the Neurosynth reverse-inference framework that meta-analytically relates striatal components to psychological states. E) The weight matrix H contains the weight of each subject's metrics onto each component, describing microstructural variation in the metrics found in the input matrix (T1w/T2w, FA, MD) between subjects. G) We used Partial Least Squares (PLS) analysis to identify patterns of covariance between the striatal components T1w/T2w, FA and MD proportions with behavioural and demographic data. PLS is a multivariate technique that analyses the association between our component-metric pairs (leftmost top) and selected behaviour/demographics (leftmost bottom) variables resulting in a set of LVs. The significance of the covariance patterns uncovered by the LVs was assessed using permutation testing while the reliability of each brain specific weight was assessed using bootstrap sampling.

sition of the input variables while prioritizing sparsity in the solution (Sotiras et al., 2015; Yang and Oja, 2010). OPNMF has already been proven effective in estimating covariance patterns in neuroimaging data while providing an easier interpretation of the results than other matrix decomposition techniques such as principal component analysis (PCA) or independent component analysis (ICA) (Sotiras et al., 2015). Briefly, NMF decomposes an input matrix ($m \times n$) into two matrices; a component matrix W ($m \times k$) and a weight matrix H ($k \times n$) where k is the number of components that needs to be specified by the user, m is the number of striatal voxels and n is the number of subjects (329) for the unimodal implementation and the number of subject-metric pairs (329 $\times$ 3) for the multimodal implementation. Here we use the same nomenclature as in Patel et al. (2020). As we are using OPNMF, our decomposition identifies k spatially distinct patterns of covariance across voxels (found in W) and across subjects and metrics (found in H). We describe below how we implemented OPNMF as well as how we interpreted the decomposition results. More theoretical concepts about OPNMF and its implementation can be found in the supplements. We examined each
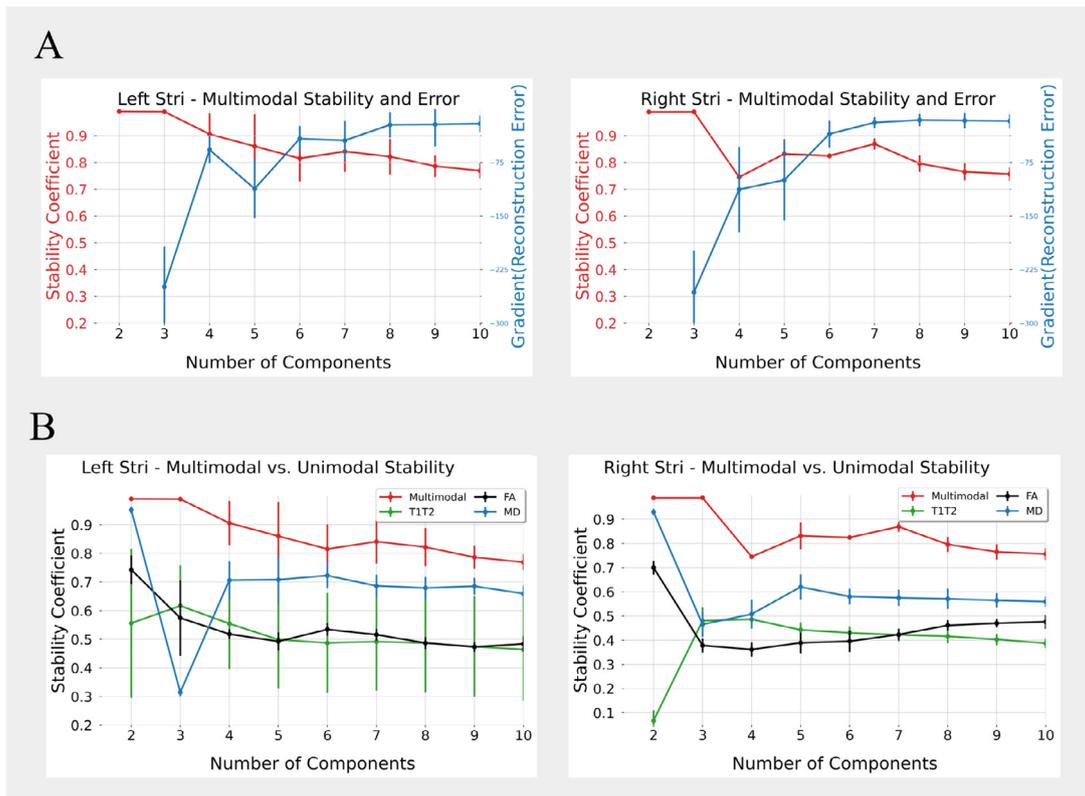
Fig. 2. Stability analyses results A) Stability score and gradient reconstruction error when performing NMF using 2 to 10 clusters. As we want to maximize the stability while minimizing the reconstruction error, we chose to use 5 components for the rest of the analysis. B) Comparison of the stability score of NMF on multimodal data (a combination of T1w/T2w, FA and MD (red)) versus unimodal data (either only T1w/T2w (green), only FA (black) or only MD (blue)) using 2 to 10 clusters. (For interpretation of the references to colour in this figure legend, the reader is referred to the web version of this article.)

microstructural measure (T1w/T2w, FA and MD) separately through a unimodal implementation of OPNMF and simultaneously through a multimodal implementation of OPNMF. More details on the implementation of the unimodal and multimodal OPNMF analyses are described below.

2.3.1. Implementation

Input matrices We used the fused left and right average striatum labels (Section 2.2.4) to perform a ROI-based extraction for the T1w/T2w, FA and MD metrics using the TractREC package. For each subject, the voxels of the striatum labels were extracted and stacked into a column vector of size (# striatal voxels × 1 subject). Therefore, we obtained voxel-wise column vectors for each subject and each of the microstructural metric (T1w/T2w, FA and MD). Hence, we obtained 3 metric vectors per hemisphere for every subject, resulting in 6 column vectors per subject. As OPNMF was applied on the two hemispheres separately, the left and right input matrices for the unimodal and multimodal OPNMF were constructed independently.

For the unimodal input matrices, we concatenated the 329 corresponding column vectors to obtain 6 (# striatal voxels × 329 subjects) matrices (per hemisphere and metric). The unimodal matrices were normalized using a standard *z*-score and shifted by the minimum value to obtain non-negativity.

For the multimodal matrices, we concatenated the unimodal matrices that were normalized to account for different scales of magnitude, resulting in one (# striatal voxels × 3 × 329) matrix per hemisphere. We then shifted all the values in our multimodal input matrices by the minimum value.

Once the input matrices were constructed, we applied the OPNMF algorithm on the left and right striatum separately. We used MatLab R2016a and some OPNMF matlab functions (Boutsidis and Gallopoulos, 2008; Halko et al., 2011; Sotiras et al., 2015; Yang and Oja, 2010).

The OPNMF algorithm was initialized using non-negative double singular value decomposition (SVD) and the following hyperparameters: max iterations = 100,000 and tolerance = 0.00001 as in (Patel et al., 2020).

2.3.2. Interpretability

OPNMF outputs a component matrix W and a weight matrix H. The (# striatal voxels × k) component matrix W describes how much each voxel contribute to a specific component. The (k × (3 × 329 subjects)) weight matrix H presents the loading of each subject's metrics onto each component, describing microstructural variation in T1w/T2w, FA and MD between subjects.

The properties of OPNMF enable us to cluster voxels via a winner takes all approach of each voxels component scores, such that each voxel was assigned to a single cluster for which it had the highest component score. Therefore, W provides spatial information about the striatal components.

For the weight matrix H, we have the subject-metric pairs as columns, component as rows and every entry represents the proportion of the metric-subject pair that contributes to each component. For a given component, the weight of a microstructural metric should be similar across subjects with some variability. Hence, H describes the importance of each component to the reconstruction of each subjects and metric, and thus tells us how T1/T2, FA,MD varies across subjects within each component.

2.4. Stability analysis

To select the optimal number of components, a stability analysis was run to assess the accuracy and spatial stability at each granularity from 2 to 10 (Patel et al., 2020). The stability analyses for the left and right striatum were performed independently.

We split our 329 subjects into two groups (a and b) of size $n_a = 164$ and $n_b = 165$. We used stratified random sampling by age and sex to avoid disproportionate subgroups in the previously mentioned demographic variables. We repeated this procedure to create 10 different splits, to obtain $10 \times 2 = 20$ groups for each hemisphere. For each split we created multimodal input matrices X_a and X_b as described in Section 2.3.1 and ran OPNMF on each split independently *(resulting in 20 splits × 2 hemispheres × 9 granularities = 360 runs)*. For each split and granularity we obtained two-component matrices W_a and W_b which are of dimension (#striatal voxels × granularity) and two weight matrices H_a and H_b of dimensions (granularity × (n_a or n_b)). The reconstruction error for each split was computed as follows:

reconstruction error A $= \|X_a - W_a H_a\|_F^2$ and

reconstruction error B $= \|X_b - W_b H_b\|_F^2$ (1)

where X_a and X_b are the input matrices of two respective groups in a split. We reported the gradient reconstruction error that corresponds to the change in the reconstruction error from a granularity k to the granularity $k + 1$. Hence, the gradient reconstruction error was computed by subtracting reconstruction error matrix of the granularity $k + 1$ with the reconstruction error matrix of the granularity k and then averaging all the differences. Then we average over all splits to get reconstruction error average and standard deviation for every granularity.

The accuracy is computed for each split by first taking two similarities matrix CW_a and CW_b of dimensions (# striatal voxels × # striatal voxels). CW_{ij} contains the cosine similarity between the components scores of voxel i and voxel j. If cosine similarity is high, it means that voxels i and j have similar component scores and that they are likely in the same cluster (Patel et al., 2020). Hence, a row i in the matrix CW_a represents the similarity of the voxel i with all the other voxels for the group a. This is the same for the matrix CW_b. Then, we computed the correlation between corresponding rows of CW_a and CW_b, to know if a certain voxel i is similar to the same group of voxels when OPNMF is applied on another group (Patel et al., 2020). If the correlation between corresponding rows of voxels was high, we conclude that the stability was high for this voxel (stability coefficient close to 1). On the other hand, instability (stability coefficient close to −1) was implied by a low correlation between corresponding rows of voxels. Finally, we took the average for all voxels and we repeated this procedure for each split to get the average and standard deviation stability coefficient for every granularity.

To assess the benefit of using multimodal data versus unimodal data, we carried out a unimodal stability analysis for the T1w/T2w, FA and MD metrics separately. As for the multimodal stability analyses, the left and right unimodal stability analyses were conducted separately, for a total of 6 unimodal stability analyses.

2.5. Microstructure-behaviour relationships

To link inter-individual variation in striatal OPNMF components to behaviour and demographics, we sought to examine their relationship to a set of behaviours and demographics available from the HCP by using subject-level weights as a measure of their specific microstructural loadings (in matrix H for each component, see Section 2.3.1). We considered all the motor-related behaviours available in the HCP test battery, as the relationship between the striatum and motor function is well known (Delong et al., 1983; Mink, 1996). This included endurance (NIH Toolbox 2-minute Walk Endurance Test), locomotion (NIH Toolbox 4-Meter Walk Gait Speed Test), dexterity (NIH Toolbox 9-hole Pegboard Dexterity Test) and strength (NIH Toolbox Grip Strength Test). We also considered cognitive tests related to impulsivity (Buckholtz et al., 2010; Dalley et al., 2008; Hariri et al., 2006), motor inhibition and cognitive control (Schouppe et al., 2014; Vink et al., 2005). Impulsivity was assessed using the delay-discount task (DD) (Estle et al., 2006; Green et al., 2007) with the area under the curve (AUC) of DD as a summary measure. Low values for the AUC suggests delayed rewards are less valuable

to the subject and vice versa (Myerson et al., 2001). Motor inhibition and cognitive control were measured by the HCP using the Flanker task from the NIH toolbox (Schouppe et al., 2014). We also considered age in years, years of education and gender as demographic measures.

2.6. Partial least squares

To associate the selected behaviours to the subjects' metric-wise component weightings, we used Partial Least Squares Correlation (PLSC). PLSC is a multivariate statistical technique that analyses the association between two sets of high-dimensional variables(Krishnan et al., 2011; McIntosh and Lobaugh, 2004; Patel et al., 2020; Zeighami et al., 2019).

In the context of the current study, we related the set of individual component weightings obtained from the H matrix in OPNMF (brain data denoted X) to the set of behavioural/demographics variables mentioned above (behaviour data denoted Y). Both X and Y have the subjects as rows and they are organized such that the rows are corresponding. For instance, the first row in Y contains the behavioural information of the subject in the first row of X. Our two initial sets X and Y are normalized using a mean-center z-score resulting in Z_X and Z_Y. Then, we compute the correlation matrix R such that $R = Z_X Z_Y^T$. Then, R is decomposed using SVD which results in a set of weighted brain saliences (U), a set of singular value and a set of weighted behavioural saliences (V) (Krishnan et al., 2011; Zeighami et al., 2019). U and V are projected back onto the normalized brain and behavioural sets Z_X and Z_Y which yields a set of uncorrelated latent variables (LVs) (Zeighami et al., 2019). Each LVs is composed of a vector of behavioural scores, a vector of brain scores and a singular value. The behavioural and brain scores contain the weights such that the original brain and behavioural variable maximally covary and the singular value represents the proportion of the covariance captured by this LV (Krishnan et al., 2011; Zeighami et al., 2019).

The significance of the patterns of covariance uncovered by the LVs can be assessed using permutation testing. Permutation testing involves randomly shuffling without replacement the rows of the brain variables matrix X to destroy its associations with the behavioural variables in Y (McIntosh and Lobaugh, 2004; Patel et al., 2020; Zeighami et al., 2019). PLSC is applied to each shuffled brain-derived matrix with the unchanged behavioural variables as described above. The singular values obtained from every permutation form a null distribution to which the original LVs' singular values can be compared and assign a non-parametric P-value (Krishnan et al., 2011; McIntosh et al., 1996; McIntosh and Lobaugh, 2004; Patel et al., 2020; Zeighami et al., 2019).

The stability, reliability of specific brain scores elements or weight are assessed using bootstrap sampling (Krishnan et al., 2011; McIntosh and Lobaugh, 2004; Zeighami et al., 2019). In bootstrap sampling, the rows of both X and Y are randomly shuffled with replacement to create a bootstrap sample (Efron and Tibshirani, 1986; McIntosh and Lobaugh, 2004). PLSC is then applied on every bootstrap sample to obtain a set of brain saliences as well as behaviour saliences vectors for every latent variable (Patel et al., 2020). We divide the brain and behavioural saliences of the original unshuffled LVs by the standard error of the bootstrap samples' saliences to obtain a bootstrap ratio (BSR). The BSR is then used to assess the significance of specific brain saliences (Krishnan et al., 2011; McIntosh and Lobaugh, 2004; Patel et al., 2020; Zeighami et al., 2019).

2.6.1. Implementation

Here, the brain matrix had dimensions (329 subjects × 3 metrics × k components) with one row for each subject and one column for each component-metric pair. The behavioural variables were stored in a 329 × 10 matrix, with the subjects as rows and the performance of selected behavioural tests along with age, sex (coded as 0/1 for M/F) and years of education as columns. Both the brain and behavioural data were z-scored manually before running PLSC. Our PLSC outputs represent a

Table 1

Participants demographics. MMSE: score on 30 of the Mini-mental state examination.

Sex	Number	Mean age (years)	Mean handedness	Mean overall cognition (MMSE)
Females	185	29.01 ± 3.63	66.59 ± 47.31	29.18 ± 0.97
Males	144	27.71 ± 3.68	59.69 ± 44.20	29.01 ± 1.08
Overall	329	28.44 ± 3.70	63.57 ± 46.04	29.11 ± 1.02

pattern of covariance between the selected behaviours and component-wise microstructural data. For the permutation testing, we computed 10,000 permuted brain matrices to construct a null distribution of singular values. We considered a threshold of $P < 0.05$ to be significant, as it corresponds to a 95% confidence that the singular value of the original LV is higher than the singular value of the permuted LV (Patel et al., 2020). As for the bootstrap sampling, we generated 1000 bootstrap samples and considered a brain salience weight with BSR > 2.58 to be significant as it corresponds to $P < 0.01$ (99% confidence) (Krishnan et al., 2011; McIntosh and Lobaugh, 2004; Patel et al., 2020).

2.7. Neurosynth image decoder

We related each component to functional MRI findings by using the Neurosynth association test framework that meta-analytically relates striatal components to brain function (Yarkoni et al., 2011). The Neurosynth database is comprised of meta-analytic functional maps for 1335 terms automatically generated from 14,371 studies. Through the Neurosynth Image Decoder, it is possible to compare any brain map to the entire Neurosynth database and thus quantitatively infer cognitive states for each uploaded map (Chang et al., 2012; Yarkoni et al., 2011). More specifically, provides posterior probability maps associated with a given term representing the likelihood that this term is being used in a study if activation is observed in the striatal voxels that we provided (see association test). As our striatal components were in the previously computed common space (Population average), we warped the components to MNI space before uploading them one by one to NeuroVault as ROI-based NIFTI images. Our MNI space striatal components are publicly available and can be used for further analysis. From the posterior probability maps provided by Neurosynth, we excluded maps with anatomical keywords to focus on cognition related terms. We also excluded maps with keywords that were either unspecific, such as "life", or redundant like "loss" and "losses".

3. Results

3.1. Data

The final sample size included 329 subjects from the Human Connectome Project Young Adult dataset as four subjects were excluded due to the lack of cognitive data. The demographic information of our participants is displayed in Table 1. We note that there is a significant difference in the mean age between males and females ($t(327) = 3.1$, $p < 0.05$), and there is no significant difference between males and females in handedness ($t(327) = 1.4$, $p > 0.1$) and overall cognition ($t(327) = 1.4$, $p > 0.1$).

3.2. Stability analysis

The results of the stability analysis are shown in Fig. 2. In Fig. 2A, the stability coefficient (red) of the multimodal OPNMF decomposition is displayed for the left and right striatum, as well as the gradient of the reconstruction error (blue) for all chosen granularities. In the right striatum, there is a net drop in the stability of the OPNMF clusters at $k = 4$, while the stability of the left OPNMF clusters slightly decay for $k \geq 3$.

The gradient reconstruction error increases as the granularity increases for both hemispheres. The gradient reconstruction error going

from $k = 3$ to $k = 4$ increases dramatically for both the left and right striatum, suggesting that there is more gain from going to $k = 2$ to $k = 3$ components than from $k = 3$ to $k = 4$ components. However, the gain in the reconstruction error of the left striatum is better than expected when going from $k = 4$ to $k = 5$. The plateau in the reconstruction error for $k \geq 6$ in both hemispheres suggests that major patterns of covariance have been captured. Hence, $k = 5$ was chosen as the optimal number of components for the left and right striatum as it is the granularity that provides the best balance between the stability coefficient and the reconstruction error (accuracy) of the OPNMF multimodal decomposition.

The results of the stability analysis comparing the multimodal versus the unimodal OPNMF decomposition with k ranging from 2 to 10 are shown in Fig. 2B. The stability coefficient of the unimodal metrics T1w/T2w (green), FA (black) and an MD (blue) is lower than the stability achieved with the multimodal decomposition (red) for both hemispheres. Due to the gain in stability of the multimodal decomposition, we decided to only conserve the 5-component multimodal solution for further analysis.

3.3. Striatal components

Fig. 3 A shows a 3D representation of the left and right striatal components, while Fig. 3B displays selected labelled and unlabelled coronal slices. The weight matrix in Fig. 3C shows the metrics proportion in each component. We only show the left weight matrix as it is almost identical to the right weight matrix. The weight matrix was divided by the mean within rows to offer better visualization of within component variation in the microstructural metrics.

- Component 1 (lilac in Fig. 3A and B) is characterized by higher values of T1w/T2w compared to MD and FA with slighty lower values of FA compared to the previous metrics (first row from the bottom in Fig. 3C). Component 1 includes the dorsal putamen as well as the dorsolateral caudate nucleus.
- Component 2 (dark magenta in Fig. 3A and B) is characterized by a high proportion of FA, followed by T1w/T2w and MD (second row from the bottom in Fig. 3C). Component 2 forms a thin capsule around the dorsal putamen and also includes the exterior lateral caudate next to the internal capsule.
- Component 3 (light mint in Fig. 3A and B) is characterized by high MD metrics compared to the proportion of T1w/T2w and FA (third row from the bottom in Fig. 3C). Component 3 is a thin cluster including the anterior and posterior medial caudate nucleus along the anterior horn of the lateral ventricle.
- Component 4 (orange in Fig. 3A and B) is characterized by lower T1w/T2w values compared to FA and MD (fourth row from the bottom in Fig. 3C). Both FA and MD in component 4 are slightly above average. This component includes the nucleus accumbens and a part of the outer ventrolateral putamen.
- Component 5 (dark green in Fig. 3A and B) is characterized by lower values of FA compared to the values of T1w/T2w and MD in this component (last row from the bottom in Fig. 3C). Component 5 includes the inner anterior ventral caudate, the medial caudate body and some part of the ventral putamen.

3.4. Partial least square analysis

To relate individuals subject's weighting from the weight matrix of OPNMF to selected behaviours and demographics, we used Partial Least
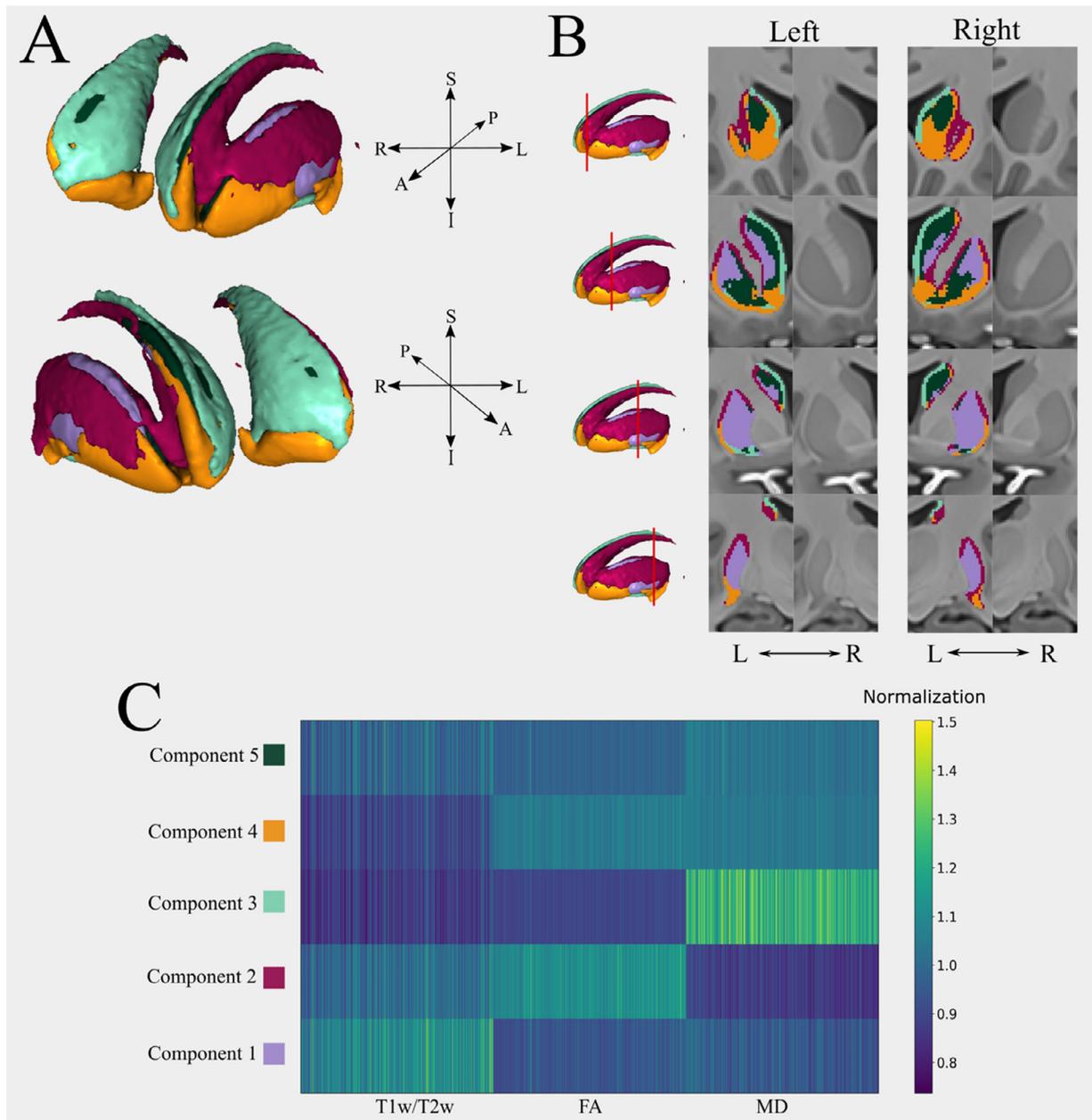
Fig. 3. Identified striatum components A) 3D rendering of the 5 components solution (A: anterior, P: posterior, S: superior, I: inferior, R: right, L: left). B) Coronal slices showing the labelled and unlabelled (side-by-side columns) left and right striatum. C) Weight matrix output from NMF of the left striatum, showing how the microstructural metrics weight into each component (the right weight matrix is almost identical). For the normalization, we divided each component (row in the matrix) by the mean value in that specific component to show within component variation in the microstructural metrics.

Square correlation analysis on the left and right hemisphere independently. Using permutation testing, we identified four significant latent variables, two for the left striatum ($p < 0.05$) and two for the right striatum ($p < 0.05$) shown in Fig. 4. Fig. 4A shows the behavioural patterns associated with the LV where the y-axis shows the behaviour and demographic measures and the x-axis shows the correlation of that behaviour/demographic and the LV. Fig. 4B shows the microstructual patterns associated with the LV where the y-axis shows the component-metric pairs and the x-axis denotes the BSR.

The first left LV (left LV1; Fig. 4A top row) explains 57% of the covariance between our two initial sets and was associated with young age ($R = -0.383$, 95% C.I. = $[-0.467, -0.300]$), male sex ($R = -0.232$, 95% C.I. = $[-0.330, -0.150]$), increased average performance on the Flanker task ($R = 0.107$, 95% C.I. = $[0.018, 0.199]$), increased

strength ($R = 0.125$, 95% C.I. = $[0.030, 0.261]$) and decreased dexterity ($R = -0.097, 95\%$ C.I. = $[-0.185, -0.013]$). The correlated microstructural features include increased MD across all 5 components, decreased FA in components 1,2 and 4 and decreased T1w/T2w in component1.

Left LV2 (Fig. 4A bottom row) explains 29% of the covariance and is associated with lower age ($R = -0.213$, 95% C.I. = $[-0.350, -0.035]$), female sex ($R = 0.186$, 95% C.I. = $[0.097, 0.314]$), decreased strength ($R = -0.190$, 95% C.I. = $[-0.308, -0.124]$) and endurance ($R = -0.136$, 95% C.I. = $[-0.230, -0.058]$). The correlated microstructural features include decreased FA in components 1, 3, 5 and decreased T1w/T2w across all components.

Right LV1 (Fig. 4B top row) explains 58% of the covariance and was mainly driven by younger age ($R = -0.227$, 95% C.I. = $[-0.335, -0.122]$), male sex ($R = -0.329$, 95% C.I. = $[-0.410, -0.267]$), in-

Fig. 4. Results of the PLS analysis, we show only the latent variables (LVs) that were significant ($p < 0.05$). The percentage next to the LV's name corresponds to the covariance explained by this LV. A) Behavioural patterns of the left LV1 (first column), left LV2 (second column), right LV1 (third column) and right LV2 (fourth column). The y-axis denotes the behavioural and demographics measures used in the analysis (DD AUC: Delay discounting area under the curve), while the x-axis corresponds to the correlation of the behaviours with the LV. B) Microstructural patterns associated with the four significant LVs identified. Here,the y-axis correspond to the component-metric pairs and the x-axis denotes the bootstrap ratio (BSR). The black line in the microstructural patterns graph represent a BSR of 2.58 (equivalent to a 99% C.I.). The colours of the bars are associated with the component (see Fig. 3C).

creased strength ($R = 0.2737$, 95% C.I. = $[0.213, 0.362]$), decreased dexterity ($R = -0.1571$, 95% C.I. = $[-0.241, -0.079]$) and AUC for both delay discounting measures DD AUC 200\$ ($R = -0.1015$, 95% C.I. = $[-0.191, -0.013]$) and DD AUC 40 000\$ ($R = -0.0734$, 95% C.I. = $[-0.160, 0.019]$). The correlated microstructural features include increased MD across all components.

Right LV2 (Fig. 4B bottom row) explained 31% of the covariance and was associated with young age ($R = 0.293$, 95% C.I. = $[0.188, 0.400]$), male sex ($R = -0.09$, 95% C.I. = $[-0.213, 0.025]$), increased endurance ($R = 0.145$, 95% C.I. = $[0.049, 0.243]$) and below average performance in the Flanker task ($R = -0.090$, 95% C.I. = $[-0.177, -0.004]$). The correlated microstructural features included increased FA across all components, increased T1w/T2w in components 1 and 3 and decreased MD in component 1.

To show the strength of the maximized correlation between the brain and behavioural variables in each latent space, we plotted the individual subject's brain PLS scores against the behavioural PLS scores for each left and right significant LV. See supplementary Fig. 4.

3.5. Decoding with neurosynth

The results of the association test performed by Neurosynth for the left and right striatal components are in Fig. 5. Some posterior probability maps were unique for certain components. Posterior probability maps with keywords related to motor function such as "motor control" and "motor response" were only associated with the first component of the left and right striatum. The same result was found for maps related to Parkinson's disease. The posterior probability map associated with the keyword "age" was only associated with the fifth right striatal component. In general, the correlations obtained for right striatal components were smaller than the correlations obtained for the left striatal components. There was also a lot of overlap within the set of posterior probability maps across components and hemispheres, but the correlation values associated with similar maps was different between components. For instance, in Fig. 5 top, we can see that both the left component 3 (light green) and the left component 4 (orange) are associated with the "reward" posterior probability map. However, the left component 4 has a bigger correlation with the "reward" map then the left component 3. The component-specific correlations values can be found in the supplement section.

Fig. 5. Neurosynth results (Top) Left striatal components Neurosynth results.(Bottom) Right striatal components Neurosynth results. Here, the colour of the words describe the components to which the posterior probability maps was related to (see Fig. 3C). The font of the word represents the Pearson correlation strength between the map of the component and the keyword related map from Neurosynth. Notice that the keywords' font were not normalized across components. Hence, the keyword with the biggest font represents the term with the biggest correlation in that component and not in all components.

4. Discussion

4.1. Overview

We identified 5 spatially distinct microstructural components for the left and right striatum using OPNMF. We also found an increase in cluster stability when performing a multimodal decomposition rather than decomposing T1w/T2w, FA and MD data independently. By using brain-behaviour PLSC, we found four significant latent variables (two for each the left and right hemispheres) relating individual subject's microstructural weightings in each component to behaviours and demographics. Finally, we also investigated how striatum clusters related to brain function using the Neurosynth database and ascertained some putative functional relationship of the specific clusters that we describe.

4.2. Spatial striatal components and microstructure

Compared to other recent parcellations of the striatum, we notice that our multimodal clusters segregate across both the caudate and the putamen which have been observed in a recent (Liu et al., 2020) multimodal parcellation of the striatum but not in other important data-driven parcellations (Janssen et al., 2015; Jung et al., 2014; Pauli et al., 2016). We also observe that the nucleus accumbens is encapsulated in its own cluster (component 4; orange) which is consistent with other striatum decompositions mentioned above.

Component 1 showed increased T1w/T2w in voxels corresponding to the dorsal putamen as well as some part of the posteromedial caudate. It has been observed that both FA and T1w/T2w are positively correlated with myelin density (Uddin et al., 2019). However, FA was shown to be a much stronger correlate of myelin content compared to T1w/T2w especially in subcortical grey matter structures (Uddin et al., 2019). Hence, the higher proportion of T1w/T2w compared to FA in component 1 might be attributed to another tissue microstructure property, like iron concentration (Péran et al., 2009; Tardif et al., 2016; Uddin et al., 2019).

Component 2 describes high FA compared to other metrics in voxels overlapping with a thin cluster along the anterior-posterior axis of lateral caudate and putamen. High FA might suggest a preferred fibre orientation in this region and myelination, although FA is sensitive to a wide range of cellular mechanism (Tardif et al., 2016; Uddin et al., 2019). High T1w/T2w signal also suggests increased myelination in this region (Uddin et al., 2019), which combined with increased FA, could indicate the presence of fibre bundles. This may capture the anterior-posterior fibre organization in the caudate nucleus and inferior-superior myelinated fibre bundles between the caudate nucleus and globus pallidus through the internal capsule, which has recently been investigated using in vivo dMRI analyses and polarized light imaging in Kotz et al. (2013).

Component 4 included voxels overlapping with the nucleus accumbens structure as defined in Haber et al. (1990) and a thin cluster around the dorsal putamen. Component 4 describes increased FA and MD compared to T1w/T2w.

Component 5 is characterized by lower MD in some part of the inner anterior ventral caudate, the medial caudate body along the voxels of component 3 and some part of the ventral putamen. Decreased MD in these regions may suggest a denser tissue microstructure (Beaulieu, 2002; Sagi et al., 2012).

The striatum has often been divided into functionally distinct regions based on corticostriatal inputs as there are no clear cytoarchitectonic parcellations of this structure. Tracing studies in non-human primates have identified a tripartite organization of the striatum based on structural connectivity to the cortex into the limbic region (ventral striatum), the association region (central striatum) and sensorimotor region (dorsolateral striatum) (Haber et al., 1995; 1994). Similar findings from tractography studies using diffusion MRI in humans have been observed in Draganski et al. (2008). The limbic region identified in (Haber et al., 2006b; 1995; 1994) overlaps with our component 4 (orange in Fig. 3) that also segregates the nucleus accumbens from the rest of the striatum. The association and sensorimotor regions from Haber et al. (2006b, 1995, 1994) do not overlap as clearly with other components as our parcellation of the limbic region and component 4. However, we still see similarities between the association striatal regions and our fifth striatal component (dark green in Fig. 3), where both overlap with some part of the anterior caudate and anterior putamen. The somatosensory striatal region in Haber et al. (2006b, 1995) corresponds the most to our component 1 (light purple in Fig. 3), comprised of the posterior putamen and posteromedial caudate.

Although our map does not exactly recapitulate this tripartite organization, we do see some similarities. This might suggest that some extrinsic structural connectivity properties of the striatum might be captured by the combination of intrinsic measures we used for our parcellation.

It is also known that the striatum contains two histochemically distinct compartments; the striosomes and matrix compartment (Flaherty and Graybiel, 1994; Graybiel and Ragsdale, 1978; Holt et al., 1997), that also differ in their input-output organization (Eblen and Graybiel, 1995; Gimenez-Amaya and Graybiel, 1991). As the striosomes patches make up only 15% (Brimblecombe and Cragg, 2017) of the adult striatum and that these patches seems to be broadly distributed in the caudate and putamen (Mikula et al., 2009), it is not clear how this binary compartmentalization would affect our decomposition. Furthermore, current MRI protocols do not allow for the direct distinction between the striosome and matrix compartment (Blood et al., 2018) and it has yet been shown if and how the striosomes and matrix compartment affect the microstructural metrics derived from MRI that we used here.

4.3. Individual-level variation in microstructure & behaviour

Microstructural components were also investigated at the individual level, where we assessed the relation between single-subject microstructure and behaviour. Using PLSC analysis, we identified two significant LVs for each the left and right striatum. Left LV1 and right LV1 displayed a similar pattern of increased MD across the left and right striatum correlated with young age, male sex and some measure of motor performance (increased strength and endurance and decreased dexterity). The negative covariance between MD and age in the pattern uncovered by the left and right LV1 is consistent with evidence of decreased MD in early adulthood in deep grey matter structures (Lebel et al., 2008). The positive relationship between age and FA which is observed in left LV1 has also been established in Lebel et al. (2008), although here, this pattern is only observed in the left striatum. As for the behaviours, we note increased strength and decreased dexterity as well as an above-average performance of the Flanker task in both left and right LV1. The motor behaviour covariance pattern in the left and right LV1 is consistent with the sex effect observed in those LVs. Indeed, increased strength and endurance as well as decreased dexterity in males have been observed in those tasks before (Bohannon et al., 2015; Hanten et al., 1999; Peters and Campagnaro, 1996)

Left LV2 described a covariance mostly related to age and sex where young females exhibited a decrease in T1w/T2w across the left striatum and a decrease in FA in the putamen and the caudate nucleus (excluding the NA and the 'outer rim' of the putamen). The positive relationship between FA and age has been observed in previous studies (Lebel et al., 2008). Recent work has also identified a positive correlation between T1w/T2w and age during early adulthood, where a bilateral increase of T1w/T2w was observed in the striatum until a peak and subsequent decline at around 50 years old (Tullo et al., 2019). The left LV2 also displayed decreased strength and endurance. As for in the left and right LV1, we note that the motor pattern in left LV2 is also consistent with the sex effect in that LV.

The right LV2 displayed an inverse age-related pattern to the left LV2, where age positively covarried with FA in the entire striatum. Age also positively covarried with T1w/T2w in the putamen and me-

dial caudate along the ventricle, while a negative covariance was observed between age and MD in the putamen. The positive relationship between age and FA in the right LV2 is consistent with findings in Lebel et al. (2008).The pattern of older age and increased T1w/T2w has also been observed in Tullo et al. (2019). In terms of behaviour and other demographics, this LV correlated with male sex, below-average performance in the Flanker task as well as increased strength and endurance.

As the female sample in this study has a slightly higher mean age than the males (mean female age = 29.01 ± 3.62, mean male age = 27.71 ± 3.67), the correlation patterns between the significant LVs with age and sex might be affected. For instance, a true correlation between an LV with age might also drive a correlation between the LV and sex or vice versa due to the previously noted bias in the sample. To investigate further the effect of sex in our LVs, we performed the same OPNMF followed by PLS on males and females independently. We found that for the left hemishpere, there was no significant difference between males and females in the striatum parcellation. Hence, we ran the PLS analysis for the left hemisphere without the sex as a variable and obtained similar LVs were the left LV1 mostly shows an effect of age and left LV2 shows an effect of the motor behaviours as seen in Fig. 4. As the right striatum parcellation was slightly different between males and females, we conducted the PLS analysis independently between males and females. We found that the microstructural partterns uncovered by the right LVs were different between males and females, probably due to the difference in the parcellation. However, the behavioural patterns were highly similar between the two groups. Indeed, the right LV1 for males and females shows mostly an effect of age and motor related behaviours while the right LV2 shows a stronger effect of impulsivity related behaviours, similar to what we show in Fig. 4 where the males and females were combined. More details on the sex specific analysis can be found in the supplement.

Moreover, relationships between brain structure and psychological traits using mass univariate approaches have been shown to have low replicability while there exist robust associations between brain structure and non-psychological traits such as age (Masouleh et al., 2019). This previously observed robust relationship between brain structure and age paired with the low variability in the HCP behavioural data might explain why we see such a strong effect of age and sex on our LVs compared to the other striatal related behaviours. In sum, we also note that the directionality of our PLSC results were as expected and we observed no laterality effects.

As discussed in another study from our group (Patel et al., 2020), the combination of OPNMF and PLS reduces the potential for false-positive as we are analyzing spatial components of voxels rather than performing univariate testing on every voxel. PLS is a multivariate technique that relates multiple variables simultaneously as opposed to multivariate testing, thus accounting for some difficulties encountered in univariate testing.There are several multivariate techniques that we could have used to relate microstructural information to behaviours. Canonical Correlation Analysis (CCA) is of particular note given its recent popularity in the literature. CCA is similar to PLS as it also seeks to find a relationship between two sets of variables by maximising the correlation between the two sets while PLS maximises the covariance (Helmer et al., 2020). PLS has been used consistently to relate neuroimaging measures to behaviour in studies relating morphometric similarity to networks defined nodal similarity to individual differences in IQ (Seidlitz et al., 2018), voxel-wise measures of atrophy to clinical measures to identify a clinical-anatomical signature of Parkinson's Disease (Zeighami et al., 2019), age dependent patterns of grey matter volume covariance across the lifespan (DuPre and Spreng, 2017), and differing structural covariance patterns between the anterior and posterior hippocampus that relate to associative memory performance (Nordin et al., 2018). Thus, we believe our use of PLS to investigate brain behaviour relationships is justifiable, and is in line with previous literature. Nonetheless, we note that although the LVs uncovered by PLS represent maximally covarying pat-

tern between the brain and behaviour variables into the latent space (Krishnan et al., 2011; McIntosh and Lobaugh, 2004; McIntosh and Mišić, 2013) and not only brain-latent variable (LV) and behavioural-LV relationship, the relationship between the brain and behavioural variable is still indirect and that the use of other multivariate techniques to define brain-behaviour dimensions should be considered in future research.

4.4. Correlation with fMRI maps

The Neurosynth reverse-inference framework found multiple correlations between output components and posterior predictive maps associated with reward, incentive and decision-making related map, which are functions that have been attributed to the striatum in previous studies (van den Bos et al., 2014; Haber et al., 2006a; 2006a; Jung et al., 2014; Pauli et al., 2016; Stott and Redish, 2014). Correlations with motor-related maps were stronger with putamen-related clusters (component 1, light purple), which is consistent with previous findings associating the putamen to somatosensory processes (Arsalidou et al., 2013; Pauli et al., 2016). We found the strongest correlation with reward-related words in the bilateral component 4, which mostly overlaps with the nucleus accumbens. This is consistent with a recent finding (Pauli et al., 2016). However, the small size of our other components (component 2, 3 and 5) resulted in a major overlap between the components and the Neurosynth maps. Although all of the words are related to previously reported striatal fucntions, the component-map correlations are not particularly specific in components 2, 3 and 5.

We also note that the correlations uncovered by the Neurosynth framework are influenced by confirmation bias. For instance, studies that looked at reward or addiction related behaviours are more likely to mention the striatum or vice-versa as it has long been thought that such associations exists.

4.5. Choice of parcellation

4.5.1. Striatal clustering

Previous parcellations of the striatum have used a combination of heuristic and contrast-based definitions. In recent years, the increased quantity and quality of available MRI data have allowed for data-driven parcellations that rely on no *a priori* assumptions on striatal organization, overcoming the limitations of past parcellation schemes. To identify spatial striatal components, previous studies have used clustering techniques such as K-means clustering (Jung et al., 2014; Parkes et al., 2017; Pauli et al., 2016), and decomposition techniques such as PCA, ICA and probabilistic modelling, such as Gaussian mixture model (Janssen et al., 2015). Amongst the variety of possible parcellation schemes, one has to be careful in the selection of a clustering/decomposition algorithm as it depends heavily on the type of data and the aims of the study.

Although OPNMF has been shown to be mathematically equivalent to the K-means algorithm (Ding et al., 2005), OPNMF was a suitable method for this study as we aimed to investigate inter-individual variability in the subjects' weightings. Sotiras et al. (2015) showed that compared to other decomposition techniques (PCA and ICA), components captured by NMF seemed to reflect relevant biological processes related to age and were less prone to overfitting. The advantages of OP-NMF interpretability have already been noted in previous studies (Patel et al., 2020; Sotiras et al., 2015; Varikuti et al., 2018). Here, we took advantage of the flexibility of NMF decomposition while capitalizing on a part-based representation of the striatum by adding the orthogonality constraint to NMF. We also note the data-driven symmetry between the components obtained in the left and right striatum.

4.5.2. Multimodal vs. unimodal

Although T1w/T2w, FA and MD are typically used in isolation, we hypothesized that since each of these measures has differential sensi-

tivity to the underlying cellular anatomy but still some overlap in their range of sensitivities (i.e they are all sensitive to myelin) (Glasser and Van Essen, 2011; Tardif et al., 2016; Tullo et al., 2019), combining them would yield more robust parcels. Here, we note that the stability of the multimodal OPNMF decomposition was notably higher than the stability of the unimodal decomposition, which provides evidence for the benefit of integrating multiple metrics to construct a parcellation.

There are multiple ways to obtain multimodal maps, however this is not a method typically employed in the literature. One way to obtain multi-modal maps is to superimpose all the parcellation schemes derived from one modality (Eickhoff et al., 2018). In this method, the final multimodal parcellation is based on the overlap of the voxels that had a similar cluster assignment in all the unimodal parcellation schemes (Eickhoff et al., 2018; Wang et al., 2015; Xia et al., 2017). Although such parcellation schemes provide useful confirmatory information, the voxels with ambiguous overlap between the distinct unimodal parcellation schemes were not necessarily included in the final map, which can lead to fragmented final multimodal parcellations (Eickhoff et al., 2018; Wang et al., 2015).

OPNMF and other similar methods, such as PCA and ICA, try to overcome this limitation by integrating multiple modalities into the parcellation, making use of the confirmatory and complementary information provided by the multiple metrics.

4.6. Limitations

An inherent limitation in this study is the lack of specificity regarding the underlying mechanism of structural and diffusion MRI derived metrics that we used. It is still not clear how specific aspects of tissue microstructure influence T1w/T2w, FA and MD. Other than myelin, the T1w and T2w signals are sensitive to the presence of macromolecules and iron concentration(Tardif et al., 2016; Uddin et al., 2019). FA and MD are also sensitive to a wide range of additional cellular properties including axonal density and orientation, water in the tissue and the presence of different cell types (Jones et al., 2013; Tardif et al., 2016). Although the combination of those microstructural metrics provides complementary and confirmatory information, it is still unclear what the underlying microstructure looks like in our identified striatal clusters. As with most non-invasive imaging studies, the resolution used in this study is subject to partial volume effects. Partial volume effects may affect metrics proportion in our striatal components, especially in components 2, 4 that are adjacent to major white matter tracts which might be contributing to the increase of FA. Partial volume effects may also play a role in the high proportion of MD in component 3 as it is adjacent to the anterior horn of the lateral ventricle. Finally, due to the nature of this research, image quality is an inherent limitation. Although manual quality control was performed at every processing and registration step of this study, we acknowledge that image quality impacts our multimodal decomposition as well as the following multivariate analysis relating microstructure to behaviours.

5. Conclusion

In this work, we used a combination of three microstructural metrics to construct a part-based decomposition of the human striatum in a healthy population using non-negative matrix factorization. By using the stability and accuracy of OPNMF decomposition, we identified 5 spatially distinct microstructural patterns for the left and right striatum separately. Then, we used partial least squares correlation to link interindividual variation in the striatal components to selected behaviours and demographics. Our findings suggest distinct microstructural patterns in the human striatum that relate mostly to demographics. Our work also highlights the gain in clusters' stability when using multimodal versus unimodal metrics. We note that the identified striatal components are associated with complex patterns of microstructure and be-

havioural variation. Further, the striatal components appear to be functionally relevant.

This work can serve as a template for examining how one can investigate subject-level variation that links brain and behaviour across numerous brain imaging measures. This may, in turn, allow for more specific interpretations of brain imaging findings that improve our mechanistic insights on brain-behaviour relationships. Further, this work could be applied in future studies of brain development and in the context of neuropsychiatric disorders to parse heterogeneity.

Ethics statement

We obtained the data in compliance with both Douglas Reseach Centre Guidlines and HCP open and restricted data use terms.

Data and code availability statement

The paper uses data from the Human Connectome Project (HCP) Young Adult dataset. Most of the neuroimaging and behavioural data are open access and may be used under the Open acess data use terms specified by the HCP. We also used restricted data that may be accessed under the HCP restricted data usage. All for data analysis associated with the current submission is already available at here, which includes the OPNMF input matrices and the scripts for the stability analyses, OPNM and PLS (including the permuation testing and bootsrap resampling). We are also planning to release the full set of neuroimaging derivatives that we used, including the metrics maps and the striatum labels on Zenodo.

Credit authorship contribution statement

Acknowledgments

Supplementary material

Supplementary material associated with this article can be found, in the online version, at 10.1016/j.neuroimage.2021.118744

References

Albin, R. L., Young, A. B., Penney, J. B., 1989. The functional anatomy of basal ganglia disorders.

Alexander, A.L., Lee, J.E., Lazar, M., Field, A.S., 2007. Diffusion tensor imaging of the brain. Neurotherapeutics 4 (3), 316–329. doi:10.1016/j.nurt.2007.05.011. Advances in Neuroimaging/Neuroethics.

Arsalidou, M., Duerden, E.G., Taylor, M.J., 2013. The centre of the brain: topographical model of motor, cognitive, affective, and somatosensory functions of the basal ganglia. Hum. Brain Mapp. 34 (11), 3031–3054. doi:10.1002/hbm.22124. https://onlinelibrary.wiley.com/doi/abs/10.1002/hbm.22124.

Avants, B.B., Yushkevich, P., Pluta, J., Minkoff, D., Korczykowski, M., Detre, J., Gee, J.C., 2010. The optimal template effect in hippocampus studies of diseased populations. NeuroImage 49 (3), 2457–2466.

Basser, P.J., Mattiello, J., LeBihan, D., 1994. Estimation of the effective self-diffusion tensor from the NMR spin echo. J. Magn. Reson. B 103 (3), 247–254. doi:10.1006/jmrb.1994.1037.

Basser, P.J., Mattiello, J., LeBihan, D., 1994. Mr diffusion tensor spectroscopy and imaging. Biophys. J. 66 (1), 259–267. doi:10.1016/s0006-3495(94)80775-1.

Beaulieu, C., 2002. The basis of anisotropic water diffusion in the nervous system-a technical review. NMR Biomed. 15 (78), 435–455.

Blood, A.J., Waugh, J.L., Münte, T.F., Heldmann, M., Domingo, A., Klein, C., Breiter, H.C., Lee, L.V., Rosales, R.L., Brüggemann, N., 2018. Increased insula-putamen connectivity in X-linked dystonia-parkinsonism. NeuroImage 17, 835–846. doi:10.1016/j.nicl.2017.10.025. https://www.sciencedirect.com/science/article/pii/S2213158217302656.

Bohannon, R.W., Wang, Y.-C., Gershon, R.C., 2015. Two-minute walk test performance by adults 18 to 85 years: normative values, reliability, and responsiveness. Arch. Phys. Med. Rehabil. 96 (3), 472–477.

van den Bos, W., Rodriguez, C.A., Schweitzer, J.B., McClure, S.M., 2014. Connectivity strength of dissociable striatal tracts predict individual differences in temporal discounting. J. Neurosci. 34 (31), 10298. doi:10.1523/JNEUROSCI.4105-13.2014. http://www.jneurosci.org/content/34/31/10298.abstract https://www.ncbi.nlm.nih.gov/pmc/articles/PMC4577570/pdf/zns10298.pdf.

Boutsidis, C., Gallopoulos, E., 2008. SVD based initialization: a head start for nonnegative matrix factorization. Pattern Recognit. 41 (4), 1350–1362. doi:10.1016/j.patcog.2007.09.010. http://www.sciencedirect.com/science/article/pii/S0031320307004359.

Brimblecombe, K.R., Cragg, S.J., 2017. The striosome and matrix compartments of the striatum: a path through the labyrinth from neurochemistry toward function. ACS Chem. Neurosci. 8 (2), 235–242. doi:10.1021/acschemneuro.6b00333.

Buckholtz, J.W., Treadway, M.T., Cowan, R.L., Woodward, N.D., Li, R., Ansari, M.S., Baldwin, R.M., Schwartzman, A.N., Shelby, E.S., Smith, C.E., Kessler, R.M., Zald, D.H., 2010. Dopaminergic network differences in human impulsivity. Science 329 (5991), 532. doi:10.1126/science.1185778. https://science.sciencemag.org/content/329/5991/532.

Burrer, A., Caravaggio, F., Manoliu, A., Plitman, E., Gütter, K., Habermeyer, B., Stämpfli, P., Abivardi, A., Schmidt, A., Borgwardt, S., Chakravarty, M., Lepage, M., Dagher, A., Graff-Guerrero, A., Seifritz, E., Kaiser, S., Kirschner, M., 2020. Apathy is not associated with reduced ventral striatal volume in patients with schizophrenia. Schizophr. Res. 223, 279–288. doi:10.1016/j.schres.2020.08.018.

Caravaggio, F., Plavén-Sigray, P., Matheson, G.J., Plitman, E., Chakravarty, M.M., Borg, J., Graff-Guerrero, A., Cervenka, S., 2018. Trait impulsivity is not related to post-commissural putamen volumes: a replication study in healthy men. PLoS One 13 (12), e0209584. doi:10.1371/journal.pone.0209584.

Chakravarty, M.M., Bertrand, G., Hodge, C.P., Sadikot, A.F., Collins, D.L., 2006. The creation of a brain atlas for image guided neurosurgery using serial histological data. NeuroImage 30 (2), 359–376. doi:10.1016/j.neuroimage.2005.09.041.

Chakravarty, M.M., Rapoport, J.L., Giedd, J.N., Raznahan, A., Shaw, P., Collins, D.L., Lerch, J.P., Gogtay, N., 2015. Striatal shape abnormalities as novel neurodevelopmental endophenotypes in schizophrenia: a longitudinal study. Hum. Brain Mapp. 36 (4), 1458–1469. doi:10.1002/hbm.22715.

Chakravarty, M.M., Sadikot, A.F., Germann, J., Bertrand, G., Collins, D.L., 2008. Towards a validation of atlas warping techniques. Med. Image Anal. 12 (6), 713–726. doi:10.1016/j.media.2008.04.003.

Chakravarty, M.M., Steadman, P., van Eede, M.C., Calcott, R.D., Gu, V., Shaw, P., Raznahan, A., Collins, D.L., Lerch, J.P., 2013. Performing label-fusion-based segmentation using multiple automatically generated templates. Hum. Brain Mapp. 34 (10), 2635–2654.

Chang, L.J., Yarkoni, T., Khaw, M.W., Sanfey, A.G., 2012. Decoding the role of the insula in human cognition: functional parcellation and large-Scale reverse inference. Cereb. Cortex 23 (3), 739–749. doi:10.1093/cercor/bhs065.

Choi, E.Y., Yeo, B.T., Buckner, R.L., 2012. The organization of the human striatum estimated by intrinsic functional connectivity. J. Neurophysiol. 108 (8), 2242–2263.

Dalley, J.W., Mar, A.C., Economidou, D., Robbins, T.W., 2008. Neurobehavioral mechanisms of impulsivity: fronto-striatal systems and functional neurochemistry. Pharmacol. Biochem. Behav. 90 (2), 250–260. doi:10.1016/j.pbb.2007.12.021. Microdialysis: recent developments.

Delong, M.R., Crutcher, M.D., Georgopoulos, A.P., 1983. Relations between movement and single cell discharge in the substantia nigra of the behaving monkey. J. Neurosci. 3 (8), 1599–1606.

Ding, C., He, X., Simon, H.D., 2005. On the equivalence of nonnegative matrix factorization and spectral clustering. In: Proceedings of the 2005 SIAM International Conference on Data Mining. SIAM, pp. 606–610.

Draganski, B., Kherif, F., Klöppel, S., Cook, P.A., Alexander, D.C., Parker, G.J.M., Deichmann, R., Ashburner, J., Frackowiak, R.S.J., 2008. Evidence for segregated and integrative connectivity patterns in the human basal ganglia. J. Neurosci. 28 (28), 7143. doi:10.1523/JNEUROSCI.1486-08.2008. http://www.jneurosci.org/content/28/28/7143.abstract https://www.ncbi.nlm.nih.gov/pmc/articles/PMC6670486/pdf/zns7143.pdf.

DuPre, E., Spreng, R.N., 2017. Structural covariance networks across the life span, from 6 to 94 years of age. Netw. Neurosci. 1 (3), 302–323. doi:10.1162/NETN_a_00016.

Eblen, F., Graybiel, A., 1995. Highly restricted origin of prefrontal cortical inputs to striosomes in the macaque monkey. J. Neurosci. 15 (9), 5999–6013. doi:10.1523/JNEUROSCI.15-09-05999.1995. https://www.jneurosci.org/content/15/9/5999.

Efron, B., Tibshirani, R., 1986. Bootstrap methods for standard errors, confidence intervals, and other measures of statistical accuracy. Stat. Sci. 54–75.

Eickhoff, S.B., Yeo, B.T.T., Genon, S., 2018. Imaging-based parcellations of the human brain. Nat. Rev. Neurosci. 19 (11), 672–686. doi:10.1038/s41583-018-0071-7.

Estle, S.J., Green, L., Myerson, J., Holt, D.D., 2006. Differential effects of amount on temporal and probability discounting of gains and losses. Memory Cogn. 34 (4), 914–928.

Flaherty, A., Graybiel, A.M., 1994. Input-output organization of the sensorimotor striatum in the squirrel monkey. J. Neurosci. 14 (2), 599–610.

Gimenez-Amaya, J., Graybiel, A., 1991. Modular organization of projection neurons in the matrix compartment of the primate striatum. J. Neurosci. 11 (3), 779–791. doi:10.1523/JNEUROSCI.11-03-00779.1991. https://www.jneurosci.org/content/11/3/779.

Glasser, M.F., Coalson, T.S., Robinson, E.C., Hacker, C.D., Harwell, J., Yacoub, E., Ugurbil, K., Andersson, J., Beckmann, C.F., Jenkinson, M., Smith, S.M., Van Essen, D.C., 2016. A multi-modal parcellation of human cerebral cortex. Nature 536 (7615), 171–178. doi:10.1038/nature18933.

Glasser, M.F., Sotiropoulos, S.N., Wilson, J.A., Coalson, T.S., Fischl, B., Andersson, J.L., Xu, J., Jbabdi, S., Webster, M., Polimeni, J.R., Van Essen, D.C., Jenkinson, M., 2013. The minimal preprocessing pipelines for the human connectome project. NeuroImage 80, 105–124. doi:10.1016/j.neuroimage.2013.04.127. Mapping the Connectome.

Glasser, M.F., Van Essen, D.C., 2011. Mapping human cortical areas in vivo based on myelin content as revealed by T1- and T2-weighted MRI. J. Neurosci. 31 (32), 11597–11616. doi:10.1523/JNEUROSCI.2180-11.2011. https://www.jneurosci.org/content/31/32/11597.

Graybiel, A.M., Grafton, S.T., 2015. The striatum: where skills and habits meet. Cold Spring Harb. Perspect. Biol. 7 (8), a021691. https://www.ncbi.nlm.nih.gov/pmc/articles/PMC4526748/pdf/cshperspect-LNM-a021691.pdf.

Graybiel, A.M., Ragsdale, C.W., 1978. Histochemically distinct compartments in the striatum of human, monkeys, and cat demonstrated by acetylthiocholinesterase staining. Proc. Natl. Acad. Sci. 75 (11), 5723–5726.

Graybiel, A.M., Rauch, S.L., 2000. Toward a neurobiology of obsessive-compulsive disorder. Neuron 28 (2), 343–347.

Green, L., Myerson, J., Shah, A.K., Estle, S.J., Holt, D.D., 2007. Do adjusting-amount and adjusting-delay procedures produce equivalent estimates of subjective value in pigeons? J. Exp. Anal. Behav. 87 (3), 337–347.

Haber, S.N., Kim, K.-S., Mailly, P., Calzavara, R., 2006. Reward-related cortical inputs define a large striatal region in primates that interface with associative cortical connections, providing a substrate for incentive-based learning. J. Neurosci. 26 (32), 8368–8376. https://www.ncbi.nlm.nih.gov/pmc/articles/PMC6673798/pdf/zns8368.pdf.

Haber, S.N., Kim, K.-S., Mailly, P., Calzavara, R., 2006. Reward-related cortical inputs define a large striatal region in primates that interface with associative cortical connections, providing a substrate for incentive-based learning. J. Neurosci. 26 (32), 8368–8376. doi:10.1523/JNEUROSCI.0271-06.2006. https://pubmed.ncbi.nlm.nih.gov/16899732 https://www.ncbi.nlm.nih.gov/pmc/articles/PMC6673798/.

Haber, S.N., Kunishio, K., Mizobuchi, M., Lynd-Balta, E., 1995. The orbital and medial prefrontal circuit through the primate basal ganglia. J. Neurosci. 15 (7), 4851–4867.

Haber, S.N., Lynd, E., Klein, C., Groenewegen, H.J., 1990. Topographic organization of the ventral striatal efferent projections in the rhesus monkey: an anterograde tracing study. J. Comp. Neurol. 293 (2), 282–298. doi:10.1002/cne.902930210.

Haber, S.N., Lynd-Balta, E., Spooren, W.P., 1994. Integrative aspects of basal ganglia circuitry. In: The Basal Ganglia IV. Springer, pp. 71–80.

Hacker, C.D., Perlmutter, J.S., Criswell, S.R., Ances, B.M., Snyder, A.Z., 2012. Resting state functional connectivity of the striatum in Parkinsons disease. Brain 135 (12), 3699–3711. doi:10.1093/brain/aws281.

Halko, N., Martinsson, P.-G., Tropp, J.A., 2011. Finding structure with randomness: probabilistic algorithms for constructing approximate matrix decompositions. SIAM Rev. 53 (2), 217–288.

Hanten, W.P., Chen, W.-Y., Austin, A.A., Brooks, R.E., Carter, H.C., Law, C.A., Morgan, M.K., Sanders, D.J., Swan, C.A., Vanderslice, A.L., 1999. Maximum grip strength in normal subjects from 20 to 64 years of age. J. Hand Ther. 12 (3), 193–200.

Hare, T.A., Tottenham, N., Davidson, M.C., Glover, G.H., Casey, B.J., 2005. Contributions of amygdala and striatal activity in emotion regulation. Biol. Psychiatry 57 (6), 624–632. doi:10.1016/j.biopsych.2004.12.038. http://www.sciencedirect.com/science/article/pii/S0006322304013812 https://www.biologicalpsychiatryjournal.com/article/S0006-3223(04)01381-2/fulltext.

Hariri, A.R., Brown, S.M., Williamson, D.E., Flory, J.D., de Wit, H., Manuck, S.B., 2006. Preference for immediate over delayed rewards is associated with magnitude of ventral striatal activity. J. Neurosci. 26 (51), 13213–13217. doi:10.1523/JNEUROSCI.3446-06.2006. https://www.jneurosci.org/content/26/51/13213.

Helmer, M., Warrington, S., Mohammadi-Nejad, A.-R., Ji, J. L., Howell, A., Rosand, B., Anticevic, A., Sotiropoulos, S. N., Murray, J. D., 2020. On stability of canonical correlation analysis and partial least squares with application to brain-behavior associations. bioRxiv, http://biorxiv.org/content/early/2020/08/25/2020.08.25.265546.abstract. 10.1101/2020.08.25.265546

Holt, D.J., Graybiel, A.M., Saper, C.B., 1997. Neurochemical architecture of the human striatum. J. Comp. Neurol. 384 (1), 1–25.

Janssen, R., Jylänki, P., Kessels, R., van Gerven, M., 2015. Probabilistic model-based functional parcellation reveals a robust, fine-grained subdivision of the striatum. NeuroImage 119, 398–405. doi:10.1016/j.neuroimage.2015.06.084. http://www.sciencedirect.com/science/article/pii/S1053811915005893.

Jones, D.K., Knösche, T.R., Turner, R., 2013. White matter integrity, fiber count, and other fallacies: the do's and don'ts of diffusion MRI. NeuroImage 73, 239–254. doi:10.1016/j.neuroimage.2012.06.081.

Jung, W.H., Jang, J.H., Park, J.W., Kim, E., Goo, E.-H., Im, O.-S., Kwon, J.S., 2014. Unravelling the intrinsic functional organization of the human striatum: a parcellation and connectivity study based on resting-state fMRI. PLoS One 9 (9), e106768. https://www.ncbi.nlm.nih.gov/pmc/articles/PMC4159235/pdf/pone.0106768.pdf.

Kotz, S.A., Anwander, A., Axer, H., Knösche, T.R., 2013. Beyond cytoarchitectonics: the internal and external connectivity structure of the caudate nucleus. PLoS One 8 (7), e70141. doi:10.1371/journal.pone.0070141.

Krishnan, A., Williams, L.J., McIntosh, A.R., Abdi, H., 2011. Partial least squares (PLS) methods for neuroimaging: a tutorial and review. NeuroImage 56 (2), 455–475. doi:10.1016/j.neuroimage.2010.07.034. Multivariate Decoding and Brain Reading.

Lebel, C., Walker, L., Leemans, A., Phillips, L., Beaulieu, C., 2008. Microstructural maturation of the human brain from childhood to adulthood. NeuroImage 40 (3), 1044–1055.

Leh, S.E., Ptito, A., Chakravarty, M.M., Strafella, A.P., 2007. Fronto-striatal connections in the human brain: a probabilistic diffusion tractography study. Neurosci. Lett. 419 (2), 113–118. doi:10.1016/j.neulet.2007.04.049. https://pubmed.ncbi.nlm.nih.gov/17485169 https://www.ncbi.nlm.nih.gov/pmc/articles/PMC5114128/.

Lehéricy, S., Ducros, M., Van De Moortele, P.-F., Francois, C., Thivard, L., Poupon, C., Swindale, N., Ugurbil, K., Kim, D.-S., 2004. Diffusion tensor fiber tracking shows distinct corticostriatal circuits in humans. Ann. Neurol. 55 (4), 522–529. doi:10.1002/ana.20030. https://onlinelibrary.wiley.com/doi/abs/10.1002/ana.20030.

Li, Y., Yuan, K., Cai, C., Feng, D., Yin, J., Bi, Y., Shi, S., Yu, D., Jin, C., von Deneen, K.M., Qin, W., Tian, J., 2015. Reduced frontal cortical thickness and increased caudate volume within fronto-striatal circuits in young adult smokers. Drug Alcohol Depend. 151, 211–219. doi:10.1016/j.drugalcdep.2015.03.023.

Liu, X., Eickhoff, S.B., Hoffstaedter, F., Genon, S., Caspers, S., Reetz, K., Dogan, I., Eickhoff, C.R., Chen, J., Caspers, J., Reuter, N., Mathys, C., Aleman, A., Jardri, R., Riedl, V., Sommer, I.E., Patil, K.R., 2020. Joint multi-modal parcellation of the human striatum: functions and clinical relevance. Neurosci. Bull. 36 (10), 1123–1136. doi:10.1007/s12264-020-00543-1.

Marquand, A.F., Haak, K.V., Beckmann, C.F., 2017. Functional corticostriatal connection topographies predict goal directed behaviour in humans. Nat. Hum. Behav. 1 (8), 0146. doi:10.1038/s41562-017-0146. https://pubmed.ncbi.nlm.nih.gov/28804783 https://www.ncbi.nlm.nih.gov/pmc/articles/PMC5549843/.

Masouleh, S.K., Eickhoff, S.B., Hoffstaedter, F., Genon, S., Initiative, A.D.N., et al., 2019. Empirical examination of the replicability of associations between brain structure and psychological variables. Elife 8, e43464.

McIntosh, A., Bookstein, F., Haxby, J.V., Grady, C., 1996. Spatial pattern analysis of functional brain images using partial least squares. NeuroImage 3 (3), 143–157.

McIntosh, A.R., Lobaugh, N.J., 2004. Partial least squares analysis of neuroimaging data: applications and advances. NeuroImage 23, S250–S263. doi:10.1016/j.neuroimage.2004.07.020. Mathematics in Brain Imaging.

McIntosh, A.R., Mišić, B., 2013. Multivariate statistical analyses for neuroimaging data. Annu. Rev. Psychol. 64, 499–525. doi:10.1146/annurev-psych-113011-143804.

Mikula, S., Parrish, S.K., Trimmer, J.S., Jones, E.G., 2009. Complete 3D visualization of primate striosomes by KChIP1 immunostaining. J. Comp. Neurol. 514 (5), 507–517. doi:10.1002/cne.22051. https://onlinelibrary.wiley.com/doi/abs/10.1002/cne.22051.

Milad, M.R., Rauch, S.L., 2012. Obsessive-compulsive disorder: beyond segregated corticostriatal pathways. Trends Cogn. Sci. 16 (1), 43–51. doi:10.1016/j.tics.2011.11.003. Special Issue: Cognition in Neuropsychiatric Disorders.

Mink, J.W., 1996. The basal ganglia: focused selection and inhibition of competing motor programs. Prog. Neurobiol. 50 (4), 381–425.

Myerson, J., Green, L., Warusawitharana, M., 2001. Area under the curve as a measure of discounting. J. Exp. Anal. Behav. 76 (2), 235–243.

Nordin, K., Persson, J., Stening, E., Herlitz, A., Larsson, E.-M., Söderlund, H., 2018. Structural whole-brain covariance of the anterior and posterior hippocampus: associations with age and memory. Hippocampus 28 (2), 151–163. doi:10.1002/hipo.22817.

Parkes, L., Fulcher, B.D., Yücel, M., Fornito, A., 2017. Transcriptional signatures of connectomic subregions of the human striatum. Genes, Brain Behav. 16 (7), 647–663. doi:10.1111/gbb.12386. https://onlinelibrary.wiley.com/doi/abs/10.1111/gbb.12386.

Patel, R., Steele, C.J., Chen, A.G.X., Patel, S., Devenyi, G.A., Germann, J., Tardif, C.L., Chakravarty, M.M., 2020. Investigating microstructural variation in the human hippocampus using non-negative matrix factorization. NeuroImage 207, 116348. doi:10.1016/j.neuroimage.2019.116348. http://www.sciencedirect.com/science/article/pii/S1053811919309395.

Pauli, W.M., O'Reilly, R.C., Yarkoni, T., Wager, T.D., 2016. Regional specialization within the human striatum for diverse psychological functions. Proc. Natl. Acad. Sci. 113 (7), 1907–1912. doi:10.1073/pnas.1507610113. https://www.pnas.org/content/113/7/1907.

Peters, M., Campagnaro, P., 1996. Do women really excel over men in manual dexterity? J. Exp. Psychol. 22 (5), 1107.

Péran, P., Cherubini, A., Luccichenti, G., Hagberg, G., Démonet, J.-F., Rascol, O., Celsis, P., Caltagirone, C., Spalletta, G., Sabatini, U., 2009. Volume and iron content in basal ganglia and thalamus. Hum. Brain Mapp. 30 (8), 2667–2675. doi:10.1002/hbm.20698. https://pubmed.ncbi.nlm.nih.gov/19172651 https://www.ncbi.nlm.nih.gov/pmc/articles/PMC6871035/.

Rolls, E., 1994. Neurophysiology and cognitive functions of the striatum. Rev. Neurol. 150 8–9, 648–660.

Rosenblatt, A., Leroi, I., 2000. Neuropsychiatry of Huntington's disease and other basal ganglia disorders. Psychosomatics 41 (1), 24–30. doi:10.1016/S0033-3182(00)71170-4. http://www.sciencedirect.com/science/article/pii/S0033318200711704.

Sagi, Y., Tavor, I., Hofstetter, S., Tzur-Moryosef, S., Blumenfeld-Katzir, T., Assaf, Y., 2012. Learning in the fast lane: new insights into neuroplasticity. Neuron 73 (6), 1195–1203. doi:10.1016/j.neuron.2012.01.025. http://www.sciencedirect.com/science/article/pii/S089662731200178X.

Schouppe, N., Demanet, J., Boehler, C.N., Ridderinkhof, K.R., Notebaert, W., 2014. The role of the striatum in effort-based decision-making in the absence of re-

ward. J. Neurosci. 34 (6), 2148–2154. doi:10.1523/JNEUROSCI.1214-13.2014. https://www.jneurosci.org/content/34/6/2148.

Schuetze, M., Park, M.T., Cho, I.Y., MacMaster, F.P., Chakravarty, M.M., Bray, S.L., 2016. Morphological alterations in the thalamus, striatum, and pallidum in autism spectrum disorder. Neuropsychopharmacology 41 (11), 2627–2637. doi:10.1038/npp.2016.64.

Seidlitz, J., Váša, F., Shinn, M., Romero-Garcia, R., Whitaker, K.J., Vértes, P.E., Wagstyl, K., Kirkpatrick Reardon, P., Clasen, L., Liu, S., Messinger, A., Leopold, D.A., Fonagy, P., Dolan, R.J., Jones, P.B., Goodyer, I.M., Raznahan, A., Bullmore, E.T., 2018. Morphometric similarity networks detect microscale cortical organization and predict inter-individual cognitive variation. Neuron 97 (1), 231–247.e7. doi:10.1016/j.neuron.2017.11.039.

Shaw, P., Sharp, W., Sudre, G., Wharton, A., Greenstein, D., Raznahan, A., Evans, A., Chakravarty, M.M., Lerch, J.P., Rapoport, J., 2015. Subcortical and cortical morphological anomalies as an endophenotype in obsessive-compulsive disorder. Mol. Psychiatry 20 (2), 224–231. doi:10.1038/mp.2014.3.

Sotiras, A., Resnick, S.M., Davatzikos, C., 2015. Finding imaging patterns of structural covariance via non-negative matrix factorization. NeuroImage 108, 1–16. doi:10.1016/j.neuroimage.2014.11.045. https://pubmed.ncbi.nlm.nih.gov/25497684 https://www.ncbi.nlm.nih.gov/pmc/articles/PMC4357179/ https://www.ncbi.nlm.nih.gov/pmc/articles/PMC4357179/pdf/nihms649302.pdf.

Stott, J.J., Redish, A.D., 2014. A functional difference in information processing between orbitofrontal cortex and ventral striatum during decision-making behaviour. Philos. Trans. R. Soc. B 369 (1655), 20130472. doi:10.1098/rstb.2013.0472. https://royalsocietypublishing.org/doi/abs/10.1098/rstb.2013.0472.

Tardif, C.L., Gauthier, C.J., Steele, C.J., Bazin, P.-L., Schäfer, A., Schaefer, A., Turner, R., Villringer, A., 2016. Advanced MRI techniques to improve our understanding of experience-induced neuroplasticity. NeuroImage 131, 55–72. doi:10.1016/j.neuroimage.2015.08.047.

Tournier, J.-D., Calamante, F., Connelly, A., 2012. Mrtrix: diffusion tractography in crossing fiber regions. Int. J. Imaging Syst. Technol. 22 (1), 53–66.

Tullo, S., Devenyi, G.A., Patel, R., Park, M.T.M., Collins, D.L., Chakravarty, M.M., 2018. Warping an atlas derived from serial histology to 5 high-resolution MRIs. Sci. Data 5, 180107.

Tullo, S., Patel, R., Devenyi, G.A., Salaciak, A., Bedford, S.A., Farzin, S., Wlodarski, N., Tardif, C.L., PREVENT-AD Research, Breitner, J.C.S., Chakravarty, M.M., 2019. MR-based age-related effects on the striatum, globus pallidus, and thalamus in healthy individuals across the adult lifespan. Hum. Brain Mapp. 40 (18), 5269–5288. doi:10.1002/hbm.24771. https://pubmed.ncbi.nlm.nih.gov/31452289 https://www.ncbi.nlm.nih.gov/pmc/articles/PMC6864890/.

Tziortzi, A.C., Haber, S.N., Searle, G.E., Tsoumpas, C., Long, C.J., Shotbolt, P., Douaud, G., Jbabdi, S., Behrens, T.E.J., Rabiner, E.A., Jenkinson, M., Gunn, R.N., 2014. Connectivity-based functional analysis of dopamine release in the striatum using diffusion-weighted MRI and positron emission tomography. Cereb. Cortex 24 (5), 1165–1177. doi:10.1093/cercor/bhs397. https://www.ncbi.nlm.nih.gov/pmc/articles/PMC3977617/pdf/bhs397.pdf.

Uddin, M.N., Figley, T.D., Solar, K.G., Shatil, A.S., Figley, C.R., 2019. Comparisons between multi-component myelin water fraction, T1w/T2w ratio, and diffusion tensor imaging measures in healthy human brain structures. Sci. Rep. 9 (1), 2500. doi:10.1038/s41598-019-39199-x.

Van Essen, D.C., Smith, S.M., Barch, D.M., Behrens, T.E.J., Yacoub, E., Ugurbil, K., 2013. The WU-minn human connectome project: an overview. NeuroImage 80, 62–79. doi:10.1016/j.neuroimage.2013.05.041. http://www.sciencedirect.com/science/article/pii/S1053811913005351.

Varikuti, D.P., Genon, S., Sotiras, A., Schwender, H., Hoffstaedter, F., Patil, K.R., Jockwitz, C., Caspers, S., Moebus, S., Amunts, K., 2018. Evaluation of non-negative matrix factorization of grey matter in age prediction. NeuroImage 173, 394–410. https://www.ncbi.nlm.nih.gov/pmc/articles/PMC5911196/pdf/nihms952495.pdf.

Veraart, J., Sijbers, J., Sunaert, S., Leemans, A., Jeurissen, B., 2013. Weighted linear least squares estimation of diffusion MRI parameters: strengths, limitations, and pitfalls. NeuroImage 81, 335–346. doi:10.1016/j.neuroimage.2013.05.028.

Vink, M., Kahn, R.S., Raemaekers, M., van den Heuvel, M., Boersma, M., Ramsey, N.F., 2005. Function of striatum beyond inhibition and execution of motor responses. Hum. Brain Mapp. 25 (3), 336–344. doi:10.1002/hbm.20111. https://www.ncbi.nlm.nih.gov/pmc/articles/PMC6871687/pdf/HBM-25-336.pdf.

Wang, J., Yang, Y., Fan, L., Xu, J., Li, C., Liu, Y., Fox, P.T., Eickhoff, S.B., Yu, C., Jiang, T., 2015. Convergent functional architecture of the superior parietal lobule unraveled with multimodal neuroimaging approaches. Hum. Brain Mapp. 36 (1), 238–257.

Westin, C.-F., Peled, S., Gudbjartsson, H., Kikinis, R., Jolesz, F.A., 1997. Geometrical diffusion measures for MRI from tensor basis analysis. In: ISMRM '97, Vancouver Canada, p. 1742.

Xia, X., Fan, L., Cheng, C., Eickhoff, S.B., Chen, J., Li, H., Jiang, T., 2017. Multimodal connectivity-based parcellation reveals a shell-core dichotomy of the human nucleus accumbens. Hum. Brain Mapp. 38 (8), 3878–3898. doi:10.1002/hbm.23636. https://www.ncbi.nlm.nih.gov/pmc/articles/PMC5685173/pdf/HBM-38-3878.pdf.

Yager, L., Garcia, A., Wunsch, A., Ferguson, S., 2015. The ins and outs of the striatum: role in drug addiction. Neuroscience 301, 529–541. doi:10.1016/j.neuroscience.2015.06.033. http://www.sciencedirect.com/science/article/pii/S0306452215005746.

Yang, Z., Oja, E., 2010. Linear and nonlinear projective nonnegative matrix factorization. IEEE Trans. Neural Netw. 21 (5), 734–749. doi:10.1109/TNN.2010.2041361.

Yarkoni, T., Poldrack, R.A., Nichols, T.E., Van Essen, D.C., Wager, T.D., 2011. Large-scale automated synthesis of human functional neuroimaging data. Nat. Methods 8 (8), 665–670. doi:10.1038/nmeth.1635.

Zeighami, Y., Fereshtehnejad, S.-M., Dadar, M., Collins, D.L., Postuma, R.B., Mišić, B., Dagher, A., 2019. A clinical-anatomical signature of Parkinson's disease identified with partial least squares and magnetic resonance imaging. NeuroImage 190, 69–78. doi:10.1016/j.neuroimage.2017.12.050. Mapping diseased brains.